



High frequency impedance characteristics of cylindrical lithium-ion cells: Physical-based modeling of cell state and cell design dependencies

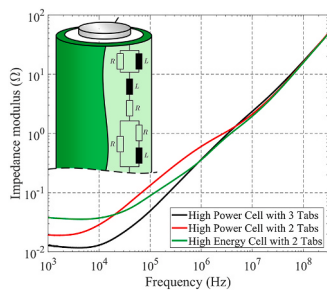
Thomas F. Landinger^{a,*}, Guenter Schwarzberger^a, Andreas Jossen^b

^a Infineon Technologies AG, Am Campeon 1-15 85579, Neubiberg, Germany

^b Technical University of Munich, Germany



GRAPHICAL ABSTRACT



ARTICLE INFO

Keywords:

Lithium ion battery
High frequency model
Cylindrical cells
Temperature influence
State of charge influence
High energy cells
High power cells

ABSTRACT

High frequency (HF) properties of lithium-ion (Li-ion) batteries receive growing attention, as an increasing number of highly dynamic loads are present in today's hybrid or battery electric vehicles (HEV, BEV). In this paper, we address the need for a better understanding of the HF characteristics of cylindrical Li-ion cells. First in literature, the impact of cell design, ambient temperature and state of charge (SOC) is investigated in a uniquely wide frequency range from 1 kHz to 300 MHz. Impedance measurements performed on eight different 18650 Li-ion cells show a strong correlation with the cell geometry including cell design (high power, high energy cell) and tab positioning along the current collectors. Moreover, the impedance response of the cells varies with temperature above 1 MHz indicating an increasing contribution of ionic current flow as the inductive reactance of the jelly roll becomes larger. SOC variations indicate only slight impedance changes below 1 MHz, most likely due to electrode volume change. The results are summarized in a physical-based HF battery model, which can be used for simulating highly dynamic battery applications such as battery power line communications (PLC) and impulsive noise investigations on the automotive high voltage (HV) power train.

1. Introduction

Electromobility is regarded as a strong driving force towards environment-friendly mobility. Its future success is directly linked to the

performance of the automotive traction battery, which needs to supply a variety of loads. Lithium-ion (Li-ion) batteries are implemented in most of today's electric and hybrid vehicles due to their high specific energy and energy density [1]. To enhance performance and safety, a battery

* Corresponding author.

E-mail address: thomas.landinger@infineon.com (T.F. Landinger).

management system (BMS) monitors the battery pack by sensors attached to the cells, which are commonly connected by a serial communication bus [2]. As this demands a huge amount of wiring, power line communication (PLC) has recently been proposed as an attractive alternative communication technique among cell sensor circuits [3–7]. Thereby, the high voltage (HV) automotive power lines including the traction battery are utilized as transmission channel, and the serial communication bus can either be omitted to save costs or used as a redundant communication system.

Predicting the performance of PLC over the traction battery requires knowledge about the battery's impedance for high frequencies in the megahertz range. On cell level, Electrochemical Impedance Spectroscopy (EIS) [8] is widely used to determine the complex-valued cell impedance over frequency. However, EIS is generally limited in frequency since regular EIS equipment mainly utilizes impedance measurement techniques, which are optimized for low-frequency relevant electrochemical process identification [8]. This makes high frequency (HF) impedance measurements and their interpretations difficult, as measurement errors such as inductive artefacts coming from the EIS equipment may distort the results [9]. As the typical frequency range of EIS lies below 10 kHz [9], we denote frequencies above 10 kHz as 'HF'. For HF cell characterization in the megahertz range, we previously proposed an alternative HF-capable impedance measurement technique, which can deal better with HF phenomena such as signal reflections and coupling effects [10]. For PLC performance prediction, it is also essential to quantify how the battery's HF impedance depends on different cell designs and how it changes over a wide range of ambient temperature and the state of charge (SOC).

Only a few publications are available dealing with the cell's behavior at high frequencies from a physical point of view. Laman et al. [11] investigated the HF properties of cylindrical cells up to 10 MHz, which had the anodic tab attached to the outermost and the cathodic tab to the innermost electrode winding¹. By adding a second anodic tab to the innermost winding, they found that the spiral geometry of the electrodes and the tab positions significantly contributes to the cell's inductance and consequently to its HF impedance.

Osswald et al. [12] confirmed these findings by assessing the inductive behavior of a cylindrical 26650 cell with EIS measurements among different tab positions along the current collectors. They concluded that the maximum impedance value at high frequencies strongly correlates with the electrode windings enclosed by the tabs.

More recently, Schindler et al. [13] investigated an 18650 cell by three electrode impedance measurements up to 1 MHz. Based on measurements and geometrical information gained from microscopical cross sections, they proposed a detailed planar transmission line model, which can predict the impact of the cell design on the battery's impedance. Beside inductive loss processes, they recognized another HF relevant resistive loss process due to radial ionic current flowing between the jelly roll layers. The study concluded that the cell design (power/energy cell) significantly changes the cell's resistive-inductive behavior for high frequencies.

In [14], Ferraz et al. proposed three high frequency cell models considering the skin effect as potential reason for the resistive HF behavior of the cell. By evaluating the cell impedance up to a frequency of 1 MHz, they found the resistive-inductive cell characteristics not to correlate substantially with SOC.

All of the cited previous studies provide valuable information about the cell's properties at elevated frequencies. However, none of them investigated frequencies higher than 10 MHz, which are of interest for PLC over the traction battery. Yet, Hoene et al. [15] investigated cell properties for frequencies higher than 10 MHz, but simplified the cell by a solid cylindrical conductor model, which does not give a detailed

insight into the cell. For this reason, in Ref. [16], we investigated the cell's resistive-inductive characteristics up to a frequency of 300 MHz. Using a novel measurement method for HF low-ohmic impedances, we were able to detect several high frequency related loss processes including the skin effect, which we summarized in a physical-based battery model. The presented approach was applied to one specific 18650 Li-ion cell, but only at a certain temperature and SOC.

To the best knowledge of the authors, no literature is available quantifying the impact of cell design, temperature and SOC on the cell's HF behavior in the megahertz range. This is critical because the battery directly affects the PLC performance, which might deteriorate for varying ambient conditions.

In this paper, we address this issue and examine how much the cell's HF impedance varies with different factors of influence. The cited previous works [11–14] already considered the cell geometry to be essential for the HF behavior of Li-ion cells. For this reason, we investigate different high power and high energy 18650 cells in a frequency range from 1 kHz to 300 MHz. Cross-sectional views of the cells are analyzed regarding tab positions and number of windings, and the cells' impedances versus frequency are obtained by vector network analyzer (VNA) measurements [17]. Moreover, we evaluate how the cells' HF impedances depend on different temperatures and SOCs and how these dependencies can be addressed by our physical-based HF battery model.

In Section 2, we present typical high frequency characteristics of cylindrical Li-ion cells found in previous literature and introduce our modeling approach. Section 3 presents the experimental setup used for the HF cell characterization. The results for different cell geometries, temperatures and SOCs are evaluated and discussed in Section 4. The paper concludes with Section 5.

2. Battery model for high frequencies

In Fig. 1a, we propose an equivalent electrical circuit (EEC) model of a single cylindrical Li-ion cell for high frequencies. The battery's typical AC impedance response is shown in the Nyquist plot in Fig. 1b. The EEC model addresses several resistive or inductive effects, which are visible at different frequency regions in the Nyquist plot. The goal of the model is to describe the frequency dependent physical effects in a compact form by lumped elements, which are frequency independent. It should be noted that the model describes the battery's AC impedance only for frequencies higher than the intercept frequency with the real axis in the Nyquist plot. It does not include slower cell dynamics such as double layer effects and diffusion, which exhibit a capacitive nature and can be found in the negative imaginary half plane of the Nyquist plot (indicated by the dashed impedance curve in Fig. 1b). Since the double layer capacitance will shunt the charge transfer reaction resistance for higher frequencies [18], this effect is also not relevant for HF battery modeling. Consequently, solely resistive and inductive loss processes determine the high frequency behavior of cylindrical cells. They can be allocated in either the electrochemical or the electrophysical domain.

It is commonly accepted that the inductive cell properties arise mainly from the spirally wound geometry of cylindrical cells [11–13]. Fig. 2a illustrates the jelly roll structure in a cross-sectional view. Copper (Cu) and aluminum (Al) current collectors are coated by the active electrode materials on both sides creating anode and cathode, respectively. To form the jelly roll, the electrodes are rolled up with separator foils placed in between [19]. Caused by this geometry, the current collectors exhibit an inductive nature, which is distributed along the collector windings and denoted as $L_{cc}'(f)$ in Fig. 2a. More specifically, $L_{cc}'(f)$ represents the self-inductance of each current collector segment and describes the voltage drop along the segments due to a time-varying current. The frequency dependency of $L_{cc}'(f)$ arises from the skin effect, which forces the current to concentrate on the outer surface of electrical conductors for higher frequencies (for further details see below).

As the cathodic and anodic current collector segments are closely attached to each other, their magnetic fields interact and mutual

¹ A graphical representation of the tab pattern can be found in Fig. 3 with reference to the Molicel IHR18650A.

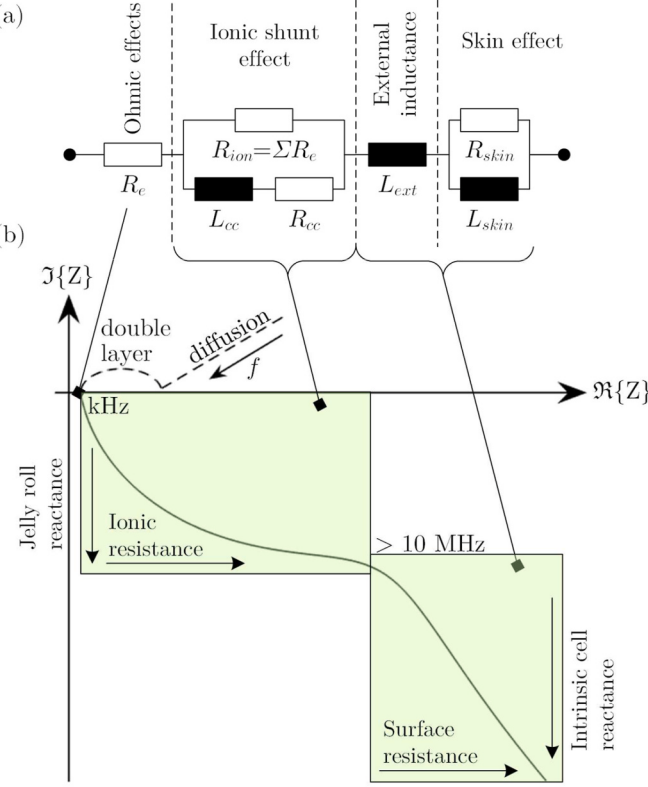


Fig. 1. (a) Physical-based high frequency EEC-model of a cylindrical Li-ion battery. The model represents the high frequency relevant loss processes, which can be found at different frequency ranges in the Nyquist plot (b). The dashed section of the cell's impedance locus indicates the low frequency relevant electrochemical effects, which are not part of the model (a).

inductive coupling was observed in previous studies [11,13]. The mutual inductance M' in Fig. 2a accounts for this phenomenon. Regarding the manufacturing of cylindrical cells, tabs are attached to the current collectors to connect the cathode to the positive cap and the anode to the negative outer casing of the cell [19]. Depending on the position of the tabs along the current collectors, the tabs will enclose more or less windings leading to a higher or lower jelly roll net inductance consisting of self and mutual inductance [12]. This will be investigated deeper in Section 4.1.

The limited conductivity per length of the current collectors is indicated by the resistor $R_{cc'}(f)$ in Fig. 2a, which is also frequency dependent due to the skin effect as previously reported in Refs. [18,20, 21]. In Ref. [22], the proximity effect was found to be a possible reason for the increasing cell resistance at high frequencies. Thereby, electrical conductors in close proximity mutually induce eddy currents forcing the overall current concentration to be higher at the non-facing surfaces of the conductors [23]. Regarding the spirally wound cell geometry, anodic and cathodic current collectors are mutually stacked. From this symmetric structure, we suppose that the proximity effect will cancel out in cylindrical battery cells and can be neglected.

The locally distributed resistor R_e' accounts for the ohmic losses occurring in the electrochemical domain and its interface to the electrophysical domain. R_e' is mainly determined by the ionic conductivity of the electrolyte, but also includes the transition resistance between active electrodes and current collectors [9,18,24]. As first component in the EEC model (Fig. 1a), the resistor R_e sums up the locally distributed ohmic resistance R_e' . The value of R_e can be estimated at the intercept frequency with the real axis of the Nyquist plot in Fig. 1b, albeit small capacitive and inductive contributions might be still present cancelling each other out [25].

The local distribution of the elements $L_{cc'}$, $R_{cc'}$, and R_e' along the

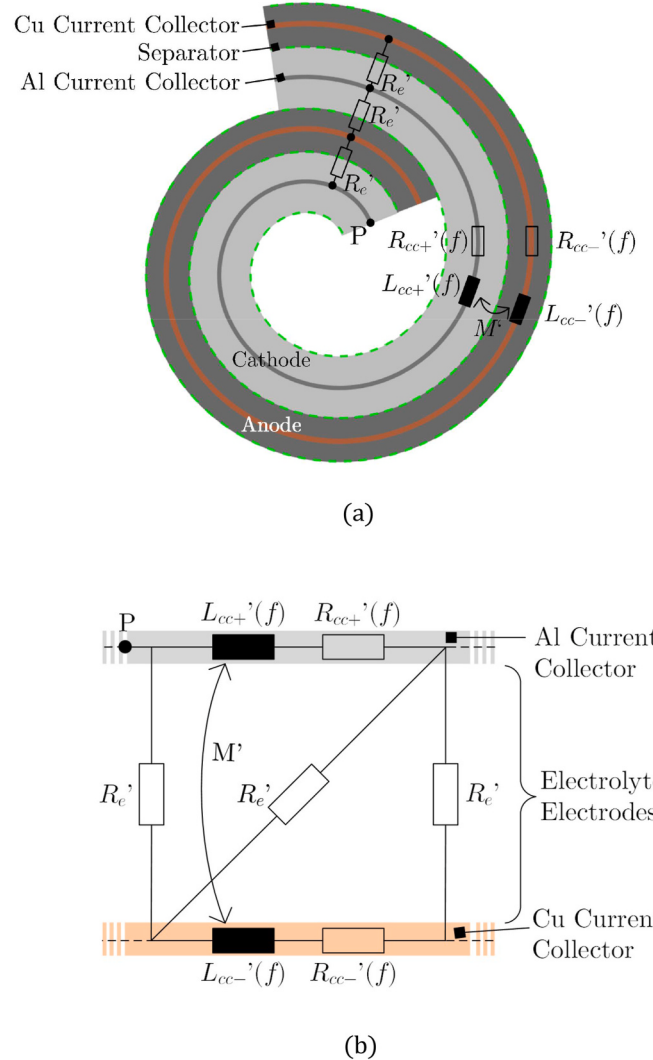


Fig. 2. Structure of a typical cylindrical Li-ion cell: (a) Cross-sectional view of the spiral geometry. (b) Representation of (a) as planar transmission line. From (b) it becomes evident that ohmic effects in the electrochemical domain are in parallel with resistive-inductive effects in the electrophysical domain. The point P in both (a) and (b) indicates the same position along the Al current collector. The locally distributed nature of the circuit elements is signified by apostrophes (') implying quantity per length. The frequency dependency of the elements $L_{cc'}$ and $R_{cc'}$ is caused by the skin effect.

spiral from Fig. 2a can be re-drawn as a planar transmission line, which is depicted in Fig. 2b. From this representation, the parallel interconnection between the electrophysical losses along the current collectors and the electrochemical losses in the electrolyte becomes obvious. This was first found in Ref. [11] and was thoroughly investigated in Ref. [13]. In the Nyquist plot (Fig. 1b), the parallel conjunction leads to a resistive-inductive impedance arc spanning frequencies from kHz up to some MHz. The arc can be explained by the increasing reactance of the current collectors for increasing frequencies. The higher the frequency, the more ionic current radially shunts the electrode windings through the jelly roll layers, seeing multiples of the electrolyte resistance R_e' [11]. Based on the observations in the Nyquist plot and the knowledge about the cell structure, we can model this ionic shunt effect by a lumped element RL parallel circuit, which is the second part of the EEC model in Fig. 1a. It comprises the net inductance L_{cc} and resistance R_{cc} of the current collectors in parallel with the ionic resistance R_{ion} , which can be seen as the total resistance of the stacked active material and the electrolyte located between the tabs.

It should be noted that although the presented cell loss processes do have an inherently distributed nature and are partly frequency dependent, we model them by lumped and frequency-constant EEC elements to obtain a compact and comprehensive battery model.

Still, the frequency dependency caused by the skin effect is included in the EEC model of Fig. 1a by another frequency constant RL circuit (R_{skin} and L_{skin}). This third EEC sub circuit accounts for the diminishing penetration depth d_{skin} (also known as skin depth) of a time varying current for increasing frequencies. For cylindrical conductors, d_{skin} can be calculated according to Ref. [26] by

$$d_{skin} = \frac{1}{\sqrt{\pi\sigma\mu f_{skin}}} \quad (1)$$

with the frequency f_{skin} , the electrical conductivity σ , and the magnetic permeability μ of the conductor. The decreased penetration depth leads to an increase in internal resistance and reactance per length according to

$$R_{int}'(f) + j2\pi f \cdot L_{int}'(f) = \frac{1}{w} \sqrt{j2\pi f \cdot \mu / \sigma}, \quad (2)$$

where $L_{int}'(f)$ is the internal inductance per length and w the circumference of the conductor. The internal resistance $R_{int}'(f)$ per length is also known as surface resistance. Equation (2) is derived in Ref. [26] by establishing the frequency dependent current density distribution inside the conductor. From (2), it can be seen that the complex internal impedance is proportional to the square root of the frequency. This would lead to an impedance curve progression with an angle of $+45^\circ$ in the Nyquist plot similar to the -45° diffusion branch described by the Warburg impedance (see Fig. 1b). However, external inductance contributions arising from the tabs and bonding wires are superimposed leading to a steeper reactance increase as visible in Fig. 1b. In the EEC model, the lumped elements describing the skin effect are denoted as R_{skin} and L_{skin} to distinguish them from the true line parameters $R_{int}'(f)$ and $L_{int}'(f)$.

Additionally for very high frequencies, the signal propagation delay due to the physical length of the cell becomes evident. When a signal propagates from one cell terminal to the other, it undergoes a phase delay, which can be regarded as the intrinsic cell inductance, which is another external inductance. The intrinsic cell inductance and the external inductance due to tabs and bonding wires are summarized by the fourth and last EEC model element L_{ext} . All EEC model components including their physical meaning are summarized in Table 1. For a deeper explanation including the model validation, the reader is referred to Ref. [16].

3. Experimental

In this work, impedance measurements were performed on eight different commercially available 18650 cylindrical Li-ion cells in the frequency range from 1 kHz to 300 MHz. The essential electrical parameters of the investigated high power and high energy cells are listed

in Table 2. The impedance measurements were carried out with an Agilent E5061B vector network analyzer (at present Keysight Technologies, Inc., USA) using the shunt-through VNA method, which is specialized for broadband low-ohmic impedance measurements [27]. The frequency span was swept with the least available bandwidth of 10 Hz to provide best accuracy, which is ensured to be below 10% according to the manual of the VNA. 1601 measurement points were recorded, which corresponds to 292 points per frequency decade. The excitation power of the VNA was chosen to be -17 dBm ($20 \mu\text{W}$), which is a tradeoff between a sufficient signal-to-noise ratio and keeping the cells within the linear region (10 mV criterion [8]). Each cell was mounted on a printed circuit board (PCB) fixture to connect it properly to the VNA by coaxial connectors and leads. By measuring a reference impedance, which we chose to be a solid copper cylinder with the same dimensions as the cell, we were able to de-embed the cell impedance from the entire measurement setup. For more details about the HF measurement method, the reader is referred to our previous work [10].

Beside the measurement method accuracy, the HF impedance deviation among cells of the same type has to be considered to provide reliable results. Four cells of the same type were characterized using the HF measurement method and found to deviate by 4% below 100 MHz and 18% between 100 MHz and 300 MHz with respect to their HF impedance. These values are well below the impedance variations presented in the results and discussion section 4 thus accounting for reliable results.

All tests were performed within the first few cycles of the cells and the SOC was kept at 50% except for the investigations on SOC dependences in Section 4.3. Thereby, electrochemical long-term changes can be excluded during the measurements.

To gain insight into the structure of the cells, each cell was investigated by X-ray computed tomography (CT) and cross-sectional scans were obtained, which are illustrated in Fig. 3. Thereby, the tab positions along the windings and the number of windings could be determined, which are presented in Section 4.1.

For temperature investigations, the cells were placed inside a Voetsch VT 7004 climate chamber (Weiss Umwelttechnik GmbH, Germany), which provides a controlled thermal environment. For each temperature setting of the chamber, a period of 2 h was chosen for temperature equilibration of the cells to obtain a homogenous temperature distribution [28]. In addition to the HF VNA impedance measurements, EIS measurements in the low-frequency region were performed at each temperature using a Zahner Electrochemical Workstation Zennium (ZAHNER-elektrik GmbH & Co. KG, Germany).

To charge and discharge the cells to certain SOC values, the ATGB 1200 battery test equipment (Batteryuniversity GmbH, Germany) was used. Table 3 summarizes the steps performed for the cell characterization at different SOCs. After a constant current/constant voltage (CCCV) charge and discharge capacity check, the cells were charged to reach the desired SOC. Subsequently, 2 h of rest were chosen for cell temperature setting. Since only frequencies higher than 1 kHz are considered, electrochemical relaxation processes are not expected to influence the impedance measurement as they only affect frequencies below 500 Hz [29].

4. Results and discussion

The section is divided into three subsections each of them discussing one factor of influence (geometry, temperature, state of charge) on the cell impedance, which have been observed during the measurements.

4.1. Geometry dependency

Four essential geometrical cell aspects reported in previous literature to affect the resistive-inductive behavior of cylindrical Li-ion cells were investigated how they change the HF cell characteristics: the number of tabs, the position of the tabs [11–13], the cell design (high power or high

Table 1

EEC battery model elements of Fig. 1a and their physical meaning.

Circuit Element	Electrochemical or -physical effect
R_e	Ohmic resistance of electrolyte and interface between active electrodes and current collector
R_{cc}	Electrical resistance of current collectors
R_{ion}	Ionic resistance of the electrolyte layers
L_{cc}	Net self-inductance of the current collectors (external inductance)
L_{ext}	Tab and bonding wire inductance, intrinsic cell inductance (external inductance)
R_{skin}	Internal (surface) resistance
L_{skin}	Internal inductance

Table 2

Electrical parameters^a and cell design parameters of the investigated 18650 Li-ion cells. For tabs located in the jellyroll, the corresponding winding number is given in parentheses, counted from inside to outside.

Cell	Nominal discharge capacity	Maximum continuous discharge current	Cathode	Anode	Number of windings	Mandrel	Group
Samsung INR18650-25R	2500 mAh	20 A	In jellyroll (15)	Cell center and can	27	No	A
Sony US18650VTC4	2100 mAh	30 A	In jellyroll (12)	Cell center and can	24	Yes	
Sony US18650VTC5	2600 mAh	30 A ^b	In jellyroll (13)	Cell center and can	24	Yes	
Panasonic NCR18650B	3350 mAh	6.2 A ^b	In jellyroll (11)	At can	17	Yes	B
Panasonic NCR18650E	2250 mAh	20 A ^b	In jellyroll (16)	At can	23	Yes	
LG INR18650 MJ1	3500 mAh	10 A	Cell center	At can	19	No	C
Molicel IHR18650A	1950 mAh	4 A	Cell center	At can	18	Yes	
A123 APR18650M1A	1100 mAh	30 A	In jellyroll (15)	In jellyroll (15)	22	Yes	D

^a Values from datasheets unless otherwise stated.

^b Information from suppliers, not verified.

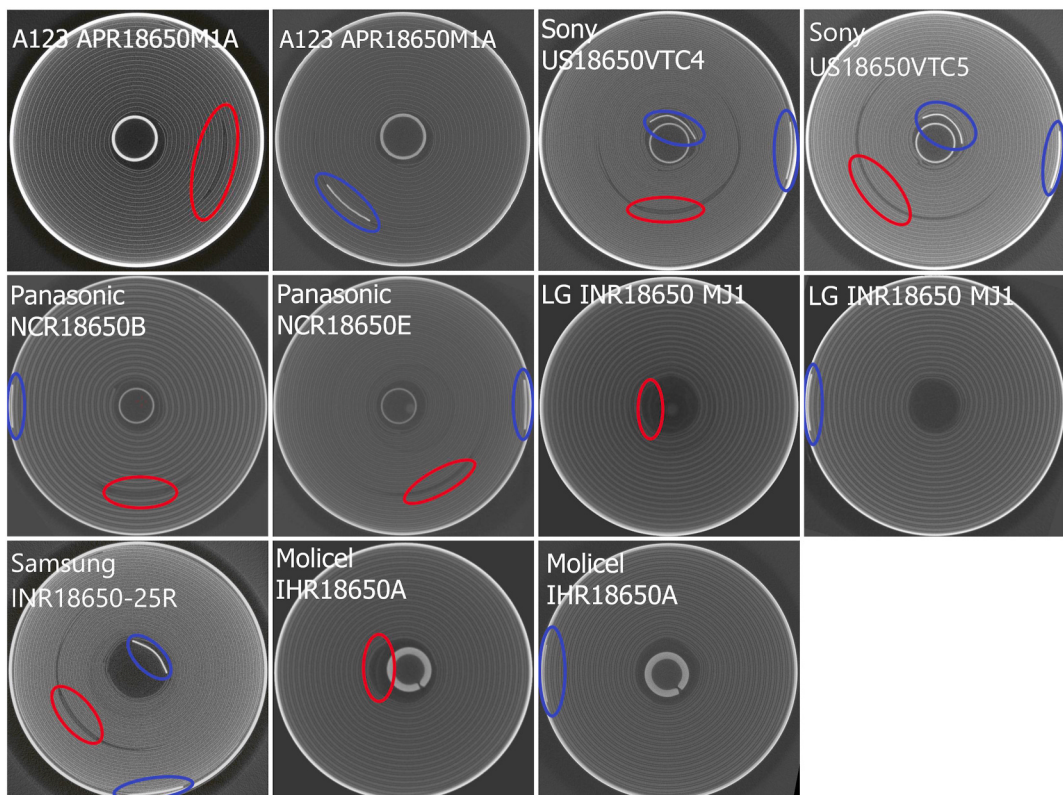


Fig. 3. CT cross sections of the investigated cells. The positions of the tabs are indicated by red (cathode) and blue (anode) markers. In some cases, two different CT scans of the cell are required to determine all tab positions. This is because the tabs are not visible together in one cross-sectional view since they do not range sufficiently along the length of the cell. All scans are viewed from the negative cell terminal. (For interpretation of the references to colour in this figure legend, the reader is referred to the Web version of this article.)

energy) [11,13,30,31] and the presence of a mandrel [12]. The cell design mainly implies the electrode thickness and number of windings [31], whereas the mandrel is a steel rod that is inserted for the winding process during manufacturing [12].

Prior to the HF measurements, CT cross sectional views illustrated in Fig. 3 were analyzed regarding tab positions, number of windings and whether a mandrel is located in the center of the cell. The resulting tab positions are marked in the CT scans and the found geometry data of the cells are summarized in Table 2. Depending on the tab positions along

the current collectors, the cells were divided into four different groups A, B, C, and D.

Before analyzing the results, the inductive nature of the spirally wound geometry of the cell has to be understood, which determines most of the overall HF cell impedance. The inductive contributions due to the cell's geometry can be separated into three parts. The first part is the spiral structure of the cell, which causes the main part of the overall cell inductance due to circumferential current flow [12,13]. To the best knowledge of the authors, no closed formula for calculating the

Table 3
Steps of the HF cell characterization for different SOCs.

Step	Parameter	End Criterion
CCCV Charge	$I_{CC} = 1C (0.5C)$, $V_{CV} = 4.2 \text{ V}$	$I_{CV} \leq 0.05C$
Pause	time t	$t = 5 \text{ min.}$
CCCV Discharge	$I_{CC} = 1C$, $V_{CV} = 2.5 \text{ V}$	$I_{CV} \leq 0.05C$
Pause	time t	$t = 5 \text{ min.}$
CC Charge	$I_{CC} = 1C (0.5C)$	$Q = 10, \dots, 90\%$
Pause	time t	$t = 2.0 \text{ h}$
HF Impedance Measurement	$P = -$ $17 \text{ dBm}, 1 \text{ kHz} \leq f \leq 300 \text{ MHz}$	Sweep end, $t = 5 \text{ min.}$

inductance of a spirally wound planar conductor is available in literature. The approximation by a set of concentric cylinders as done in Refs. [11,13] was reported in Ref. [32] to be valid only when little current flows in circumferential direction. This applies to metallized film capacitors, where the electrode face ends are continuously connected to the tabs by a metal spray [32] leading to a current flow solely in longitudinal direction. However, this is not the case for cylindrical battery cells, where the tabs are connected to the current collectors only at specific points along the windings.

The second part addresses the inductive coupling between positive and negative current collectors, which is illustrated in Fig. 4. Depending on the tab positions, the current in both collectors is in either parallel or antiparallel relationship and induces a positive or negative voltage drop with respect to the voltage drop caused by the collector's self-inductance L_+ or L_- . If the currents are in parallel as in Fig. 4a, the mutual coupling inductance M adds up the self-inductance of the current collectors and the net inductance of the segment is

$$L_{par} = (L_+ + M) \parallel (L_- + M). \quad (3)$$

For the readers' convenience, we depicted the detailed mathematical part of equations (3)–(5) in the appendix part of this work and only give the final form - relevant in the following – here.

Regarding the other case, when the tabs are located face-to-face at one end of the collectors as indicated in Fig. 4b, the currents are in opposite directions (their sum is zero) and M gets a negative sign.

As reported in Ref. [13], the inductive coupling factor $k := M/\sqrt{L_+ L_-}$ between the current collectors is close to 1 due of the tight alignment of the electrode layers. Supposing equal currents on both collectors, a coupling factor of nearly 1, and equal inductance values of L_+ and L_- inserted in (3), the net inductance of the segment from Fig. 4a is

$$L_{par} \approx (2L_+) \parallel (2L_+) = L_+, \quad (4)$$

whereas in the case of antiparallel current flow as in Fig. 4b, the net inductance is close to zero:

$$L_{par} \approx (L_+ - L_-) + (L_- - L_+) = 0. \quad (5)$$

Regarding Fig. 4, the current density changes along the current collectors and is different for (a) and (b). However, as the coupling factor k is close to 1, this has no impact on the net inductance of the segments.

The third part of the geometry-caused inductive contribution is the physical length of the cell, which causes a current flow in longitudinal direction from one battery terminal to the other. It can be approximated by the inductance of a hollow cylinder, which can be calculated by

$$L_{cyl} = \frac{\mu_0}{2\pi} l \left(\ln \left(\frac{2l}{r} \right) - 1 \right). \quad (6)$$

Equation (6) was originally given by Rosa [33] developing the concept of partial inductance, and can be found in inductance textbooks such as in Ref. [34]. Using the cell's length $l = 6.5 \text{ cm}$ and radius $r = 9 \text{ mm}$ and the permeability $\mu_0 = 4\pi \cdot 10^{-7} \text{ H/m}$, equation (6) yields an inductance of 21.7 nH . This so-called intrinsic cell inductance causes an additional phase shift especially in the very high frequency range

above 100 MHz, where the signal wavelength reaches the dimensions of the 18650 cell.

4.1.1. Cell impedance measurements

Fig. 5 presents the HF impedance measurement results of the investigated cylindrical Li-ion cells. The results are separated into four sub-figures a,b,c,d according to the aforementioned four groups of cells A,B,C, and D with different tab patterns as indicated. In Fig. 5d, beside group D, also one representative cell from each of the other groups A,B,C is added to allow a comparison among different groups.

For each 18650 cell, the HF EEC battery model of Fig. 1a was fitted to the corresponding impedance measurement using the randomize and simplex algorithms provided by EC-Lab® Software (BioLogic, France). The relevant fitted inductance and ohmic resistance values are summarized in Table 4. Since the chosen battery model aims to describe the HF behavior in a highly compact manner yet with physical meaning, there remains a deviation between measurement and model. A typical model fit and its mean square deviation from the measurement is pictured in the appendix. Since the time constants of the loss processes are largely distinct from each other, overfitting issues did not occur. For the following analysis, the frequency range is separated into three ranges: Low frequency range I (1 kHz–20 kHz), high frequency range II (20 kHz–10 MHz) and very high frequency range III (10 MHz–300 MHz).

As visible in the Bode plots of Fig. 5a–d, depending on each cell's ohmic resistance, the impedance magnitude starts at low-ohmic values in frequency range I and strongly increases due to the resistive-inductive properties of the cell for higher frequencies in range II and III. This can also be seen from the impedance phase reaching almost an angle of 90° for 300 MHz. Frequency range II highlights the different inductive properties of different cell designs and tab patterns, whereas in range III, interestingly all cells exhibit more or less the same impedance magnitude and phase. The observations in range III match the fitted values of the external inductance L_{ext} in Table 4, which are only slightly higher than the hollow cylinder inductance of 21.7 nH calculated by (6) using the 18650 cell diameter. From this, we can conclude that above approximately 70 MHz, the cell design and tab patterns do not significantly affect the HF impedance anymore and the current is forced towards the outermost winding of the cell, where it sees the lowest possible cylinder inductance.

As the inductive parts contribute much more to the impedance growth than the resistive parts, the Nyquist plots of Fig. 5a–d also highlight the increase separated in real and imaginary part. From the Nyquist plots, we can allocate the resistive-inductive impedance arc in frequency range II revealing the ionic shunt effect. The arc broadens for cells with higher ohmic resistance because the ionic currents see more resistance when shunting the electrode layers. In frequency range III, the resistance of the cells still increases, which can be addressed to the skin effect. The characteristic bending in the Nyquist plots marks the transition from frequency range II to III.² The impedance bending is most probably due to the settling ionic shunt effect and the initiating skin effect. Solving (1) for the skin frequency f_{skin} using a typical Cu current collector ($\sigma = 58 \cdot 10^6 \text{ S/m}$, $\mu = \mu_0 = 4\pi \cdot 10^{-7} \text{ H/m}$, $d_{skin} = 13 \mu\text{m} = d_{Cu}$) leads to $f = 25 \text{ MHz}$. Due to the definition of the skin depth being the depth where the current density has decreased to $1/e \approx 37\%$ of the surface value, the skin effect is expected to be already noticeable at frequencies below 25 MHz. This matches our observations in the Nyquist plots, where the skin effect becomes obvious between 10 and 20 MHz. As copper has a much higher conductivity than aluminum ($\sigma = 3.7 \cdot 10^6 \text{ S/m}$), we conclude that the anodic current collector mostly defines the skin

² One exception is the A123 APR18650M1A, where the bending point is at a much higher frequency. Although both tabs are located inside the jelly roll, they are not located quite face to face as can be seen from the corresponding cross sections in Fig. 3. This might cause an increased ionic current flow leading to the visible impedance arc.

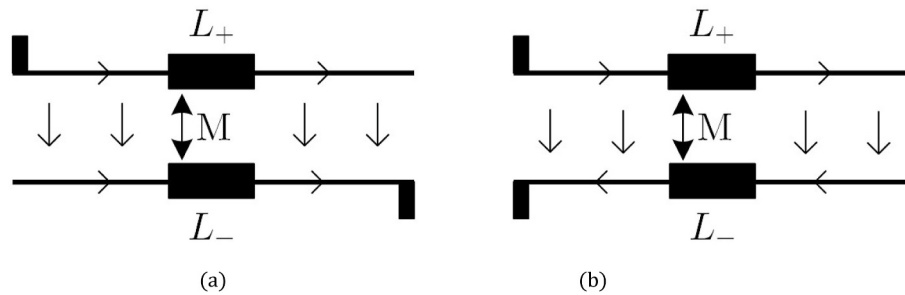


Fig. 4. Mutual coupling between the current collectors for parallel (a) and anti-parallel (b) current flow depending on the tab position.

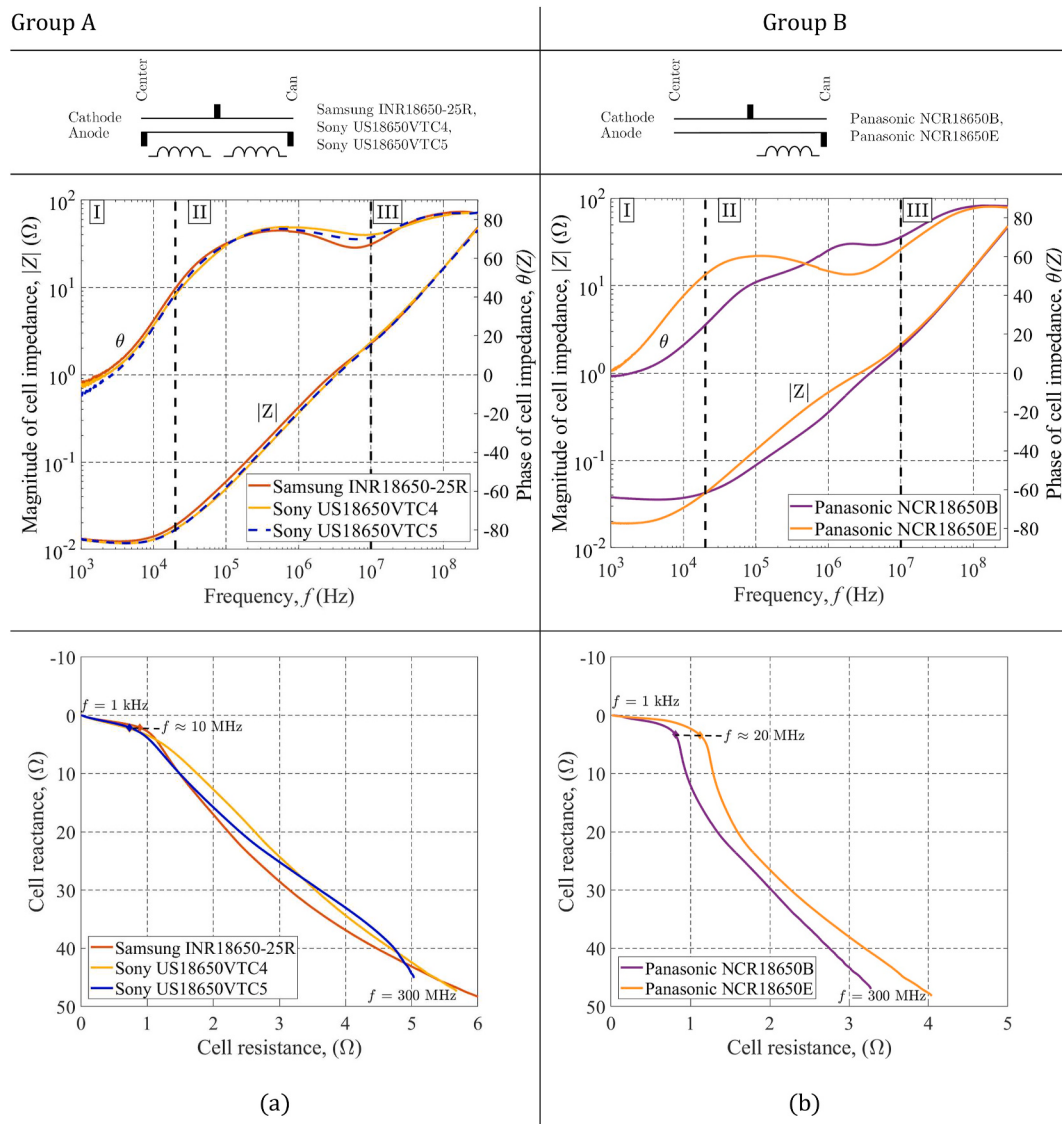


Fig. 5. HF impedance measurement results of eight different 18650 Li-ion cells grouped according to their tab patterns as indicated in (a-d). A Bode plot and a Nyquist plot illustrate the results for each group. In (d), one cell of each group/tab pattern is added enabling a comparison among different groups.

effect characteristics in frequency range III. The varying fitted values of the internal inductance L_{skin} in Table 4 may be due to different current collector thicknesses of the cells, but may also be due to fitting variance. For a deeper inspection, the thickness of the collectors of all cells would need to be determined, which is beyond the scope of this work. How the different cell geometries further affect the HF cell impedance is

discussed in the following.

4.1.2. Tab position

Regarding the mixed group results shown in Fig. 5d, the Bode plot reveals how different tab positions along the current collectors affect the cell impedance. As stated above, frequency range II provides insight on

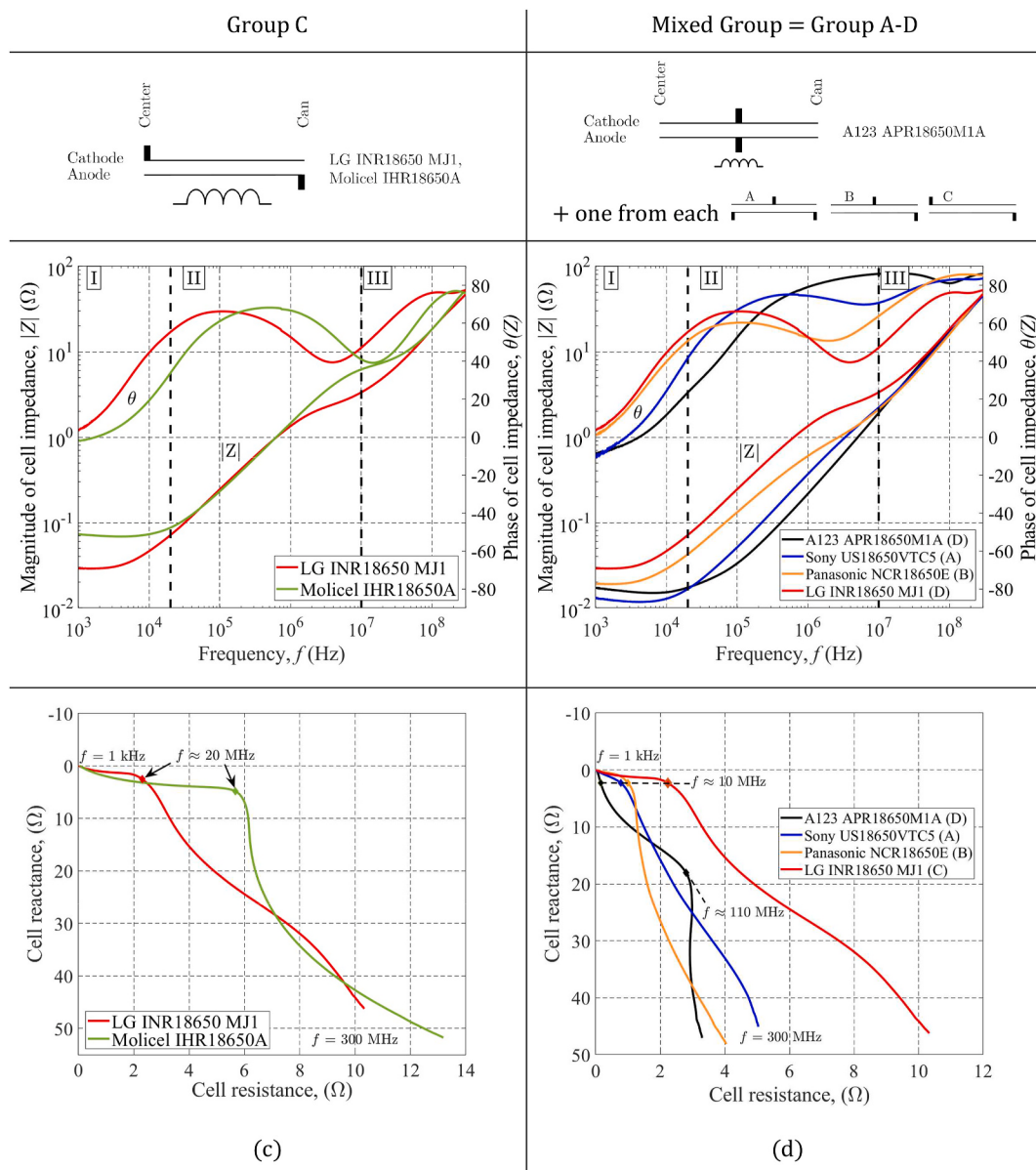


Fig. 5. (continued).

Table 4

Measured ohmic resistance and fitted inductance model parameters of the EEC model (Fig. 1a).

Cell	R_e ($\text{m}\Omega$)	L_{cc} (nH)	L_{skin} (nH)	L_{ext} (nH)	Group
Samsung INR18650-25R	12.6	38.6	4.6	22.4	A
Sony US18650VTC4	12.0	22.2	4.7	21.9	
Sony US18650VTC5	11.9	27.6	4.5	22.2	
Panasonic NCR18650B	29.3	33.1	3.4	22.0	B
Panasonic NCR18650E	19.4	81.5	3.8	22.0	
LG INR18650 MJ1	29.5	226.8	8.9	21.3	C
Molicel IHR18650A	70.4	197.3	5.5	23.2	
A123 APR18650M1A	15.2	14.8	7.6	24.3	D

how geometry aspects change the impedance characteristics. In case of Fig. 5d, range II indicates that the cell impedance is higher the more distance lies between the positive and negative tabs. In case of the A123 APR18650M1A (group D), the tabs are placed in the middle of the jelly roll (see Fig. 3) and the cell shows the least impedance, followed by

groups C, B and A. Because the complex impedance Z is linked to the inductance L via $Z = j2\pi f_0 L$, a higher impedance at a certain frequency f_0 in the Bode plot corresponds to a higher inductance at f_0 . From this, we can conclude that more windings enclosed by the tabs lead to a higher overall jelly roll inductance, which is in accordance with the previous findings in Refs. [11–13]. This is also confirmed by the fitted L_{cc} values in Table 4, which increase from 14.8 nH in case of the A123 APR18650M1A to 226.8 nH in case of the LG INR18650 MJ1, which has the highest jelly roll inductance among the investigated cells.

4.1.3. Number of tabs

Comparing the representative cells of group A (three tabs) and B (two tabs) in the Bode plot of Fig. 5d, group A exhibits slightly lower impedance values in frequency range II. Also the fitted jelly roll inductances L_{cc} (Table 4) of the cells from group A are lower than those from group B except for the Panasonic NCR18650B, which has significantly less windings (see Table 2). When looking back at the inductive coupling illustrated in Fig. 4 and equations (4) and (5), one can conclude that only collector segments with parallel current flow contribute to the jelly roll inductance. Consequently, in case of group B, only the collector

segments in between the tabs are essential for the overall inductance. Another reason for the negligible inductance of segments not being between tabs as drawn in Fig. 4b, could be a non-uniformly decreasing current density with increasing distance to the tabs, which was found in Ref. [12]. The three-tab arrangement of group A can be seen as two parallel inductances as drawn below the tab pattern in Fig. 5a, whose net inductance is smaller than a single inductance. Therefore, we can conclude that more tabs reduce the inductance of the spirally wound cell.

When looking at the Nyquist plot of Fig. 5d, the Sony US18650 VTC5 (group A) exhibits a higher real part than the Panasonic NCR18650E (group B) for very high frequencies. As described in Section 2, the ionic shunt effect leads to current flowing radially between the jelly roll layers. Therefore, the smaller real part may be caused by the smaller radial distance between the tabs in case of the Panasonic cell, which is visible in the corresponding cross sections in Fig. 3.

4.1.4. Cell design (high energy, high power)

The investigated 18650 Li-ion cells are either optimized for high power capability or high energy density, which can be deduced from the electrical parameters given in Table 2. To examine the influence of the cell design, a high energy (NCR18650B) and a high power (NCR18650E) cell by the Panasonic Energy Company are compared, whose impedance results are given in Fig. 5b (group B). To achieve a high energy density in cylindrical Li-ion cells, the electrodes are typically thicker than for high power cells [31,35], which is visible in the CT cross sections of the Panasonic cells in Fig. 3. Since thicker electrodes experience higher losses, the ohmic resistance R_e is higher thereby limiting the maximum power [35]. In contrast, high power cells like the Panasonic NRC18650E have thin electrodes to minimize R_e . The thin electrode layers lead to a higher amount of windings for high power cell as visible in Fig. 3. Therefore, we expect higher ohmic and inductive losses for high power cells at high frequencies, which was also reported in Ref. [13]. When looking at the results in Fig. 5b, the Bode plot reveals the different frequency characteristics. In frequency range I, the high power cell exhibits a smaller impedance, which increases faster than the high energy cell leading to a higher impedance in range II. In range III, both cells have quite similar impedance characteristics. We can conclude that the higher amount of windings of the high power cell leads to an increased current collector inductance L_{cc} (see Table 4), which causes the impedance to increase faster with frequency than for the high energy cell. These findings are in accordance to a cylindrical coil (solenoid), where the inductance increases with more windings ($L \propto N^2$) [36]. The mechanism behind can be explained by magnetic flux linkage, which increases with additional windings and thus does the inductance. For more information, the reader is referred to electromagnetics textbooks such as [36]. From the Nyquist plot, also the increased ohmic losses at high frequencies due to more windings become visible.

4.1.5. Presence of mandrel

As visible in Fig. 3 and summarized in Table 2, several of the investigated Li-ion cells have a center pin also called mandrel, which is used for the winding process of the jelly roll during manufacturing. Looking at the cell group A, the mandrel's influence on the HF cell behavior can be assessed since there are three cells with quite similar geometries except for the mandrel. As there is no significant difference visible between the impedance results in Fig. 5a, it is expected that the mandrel has no influence on the HF cell impedance. The slightly higher impedance of the Samsung INR18650-25R in frequency range II in the Bode plot of Fig. 5a is most likely due to the higher amount of windings as listed in Table 2.

4.2. Temperature dependency

For temperature investigations, two 18650 cells from Table 2 were

selected having different electrical and chemical properties: the Samsung INR18650-25R having a cathode composed of nickel manganese cobalt (NMC³) and the Panasonic NCR18650B having a nickel–cobalt–aluminum (NCA³) composed cathode. In Fig. 6, Nyquist plots (a, b) and a Bode plot (c) illustrate the cell impedance for different temperatures. Fig. 6b and c only include the impedance curves of the Samsung cell to ensure readability, yet the impedance curves of the Panasonic cell show comparable results. In Fig. 6a, the real part of the impedance and the ohmic resistance at the intercept frequency significantly increase with decreasing temperature. Moreover, the transition from capacitive to inductive cell behavior is shifted to higher frequencies, which can be seen from the phase progression in Fig. 6c. These observations were also reported in previous literature [12,37,38] and can be accounted for by reduced charge transfer kinetics [39] and lowered electrolyte conductivity [40]. The latter dominates the temperature behavior of the ohmic resistance [41], whereas the conductivity variation of the metallic current collectors is negligible in the regarded temperature range [42]. Considering the impedance modulus in Fig. 6c, the curves for different temperatures overlay exactly in the entire frequency range except of a remarkable 15 MHz band centered around 10 MHz as indicated by the magnifying inset. In this band, the impedance significantly increases for lower temperatures suggesting a temperature effect dominated by the electrolyte conductivity. As found in the geometry section 4, the highlighted 15 MHz band is the frequency region, where ionic branch currents start flowing radially across the electrode layers shunting the current collector segments. Based on these findings, we suppose that the ionic branch currents see more or less electrolyte resistance depending on the temperature, which leads to the visible impedance spread in Fig. 6c. This can also be observed in the HF Nyquist plot of Fig. 6b, where the resistive-inductive impedance arc broadens for decreasing temperature leading to a higher real part of the cell impedance. Regarding the phase progression in Fig. 6c, we see that the characteristic phase minimum at some megahertz shifts to higher frequencies for lower temperature. From this, we assume that the ionic shunt effect is also shifted to higher frequencies for decreasing temperatures. This is because the higher electrolyte resistance forces the current to keep flowing on the collectors, and ionic branch currents caused by increasing collector reactance tend to initiate at higher frequencies. For frequencies above the highlighted 15 MHz band, the impedance modulus in Fig. 6c seems to be equal again for all temperatures. However, the strong increase in the imaginary part overshadows the impedance's real part in the Bode plot. From the HF Nyquist plot in Fig. 6b, it becomes clear that the real part remains temperature dependent also for higher frequencies.

The temperature dependency of the resistance of the electrolyte can be approximated by an Arrhenius behavior [40,42,43].

$$R_{ion} = \lambda \cdot e^{\frac{E_A}{k_B T}}, \quad (7)$$

with the activation energy E_A , the proportionality constant λ (Ω^{-1}) and the Boltzmann constant k_B . In Fig. 6d, impedance and resistance values of the investigated cells measured at 10 MHz are depicted in an Arrhenius plot. In addition, the fitted ionic resistance R_{ion} of the HF-EEC model describing the resistive-inductive impedance arc is added to Fig. 6d. All impedance curves exhibit an Arrhenius-like behavior and their activation energies lay between 0.04 eV and 0.12 eV as marked in the figure. The fitted R_{ion} has a significantly higher E_A than the measured values, likely because it models the ionic shunt effect over a broad frequency band. The measured values only represent one frequency point and do not account for the frequency shift of the entire ionic shunt effect for varying temperatures. There is also an Arrhenius-like behavior observed for the impedance modulus. This can be confirmed by the fact that the real part of the impedance is dominated by the temperature dependent

³ Values from material safety datasheets.

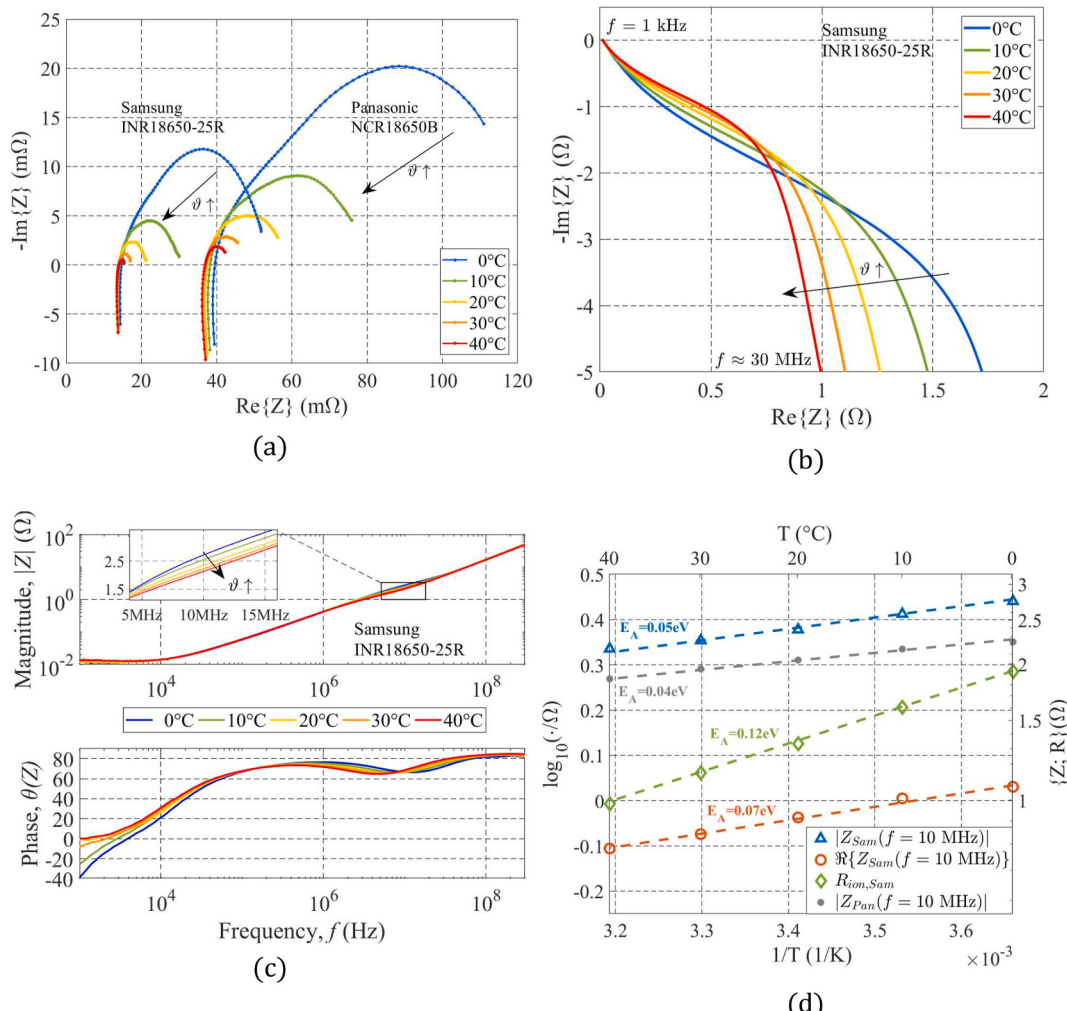


Fig. 6. Temperature dependency of the cell impedance for two different cylindrical 18650 Li-ion cells: EIS Nyquist plot (a) of both cells, HF Nyquist plot (b) and Bode plot (c) of Samsung INR18650-25R for different temperatures. Arrhenius plot (d) of selected impedances, namely Z_{Sam} (impedance of Samsung cell), its real part $\Re\{Z_{Sam}\}$, and Z_{Pan} (impedance of Panasonic cell) at 10 MHz. In addition, the fitted ionic shunt resistor $R_{ion,Sam}$ of the EEC HF model is depicted for the Samsung cell.

electrolyte resistance, whereas the imaginary part is mostly determined by the inductive cell properties, which are nearly temperature independent. The determined activation energies are in the same order of magnitude as previously found in Ref. [42], where the authors attributed the temperature dependency of the ohmic resistance mainly to the temperature dependent electrolyte conductivity. In conclusion, the found Arrhenius-like behavior underlines that the temperature-dependent electrolyte conductivity is mainly accountable for the HF impedance variation with temperature by 20% from 0 °C to 40 °C at frequencies above some megahertz.

4.3. State of charge dependency

For PLC, it is important that the communication performance does not vary with different SOCs. Therefore, the dependency of the HF cell impedance on SOC was investigated based on SOC variations (10%–90%) of the same cells already considered for the temperature investigations in Section 4.2. Fig. 7 illustrates the impedance measurement results for different SOCs in a Nyquist plot (a) for both cells and two Bode plots (b, c) each for one cell. In Fig. 7d, the SOC dependency of the cell impedance for selected frequencies is depicted. Regarding the Samsung INR18650-25R, both the Nyquist (Fig. 7a) and the Bode plot (Fig. 7b) do not indicate any significant impedance change within the considered SOC range. There are little variations in the Nyquist plot

most likely caused by measurement uncertainty. As found in literature, the cell impedance is nearly independent of SOC for frequencies higher than the intercept frequency [9,37,42,44]. It is also reported, that the ohmic resistance of the cell remains constant [9] or exhibits only small changes [9,38,43]. Interestingly, the Panasonic NCR18650B behaves differently from the Samsung cell as can be seen from Fig. 7a and d. The ohmic resistance increases by 15% from 33 mΩ (90% SOC) to 38 mΩ (10% SOC). Moreover, the cell impedance increases for low SOC values over a wide frequency range up to 1 MHz, mainly due to an increase in the real part (see magnifying inset of Fig. 7a). However, for higher frequencies, no SOC dependency can be observed. In contrast to the cyclic conditioning listed in Table 3, in a second experiment, the SOC was additionally adjusted by fully charging and then discharging the cell until reaching the desired SOC. This lead to the same results as for the procedure according to Table 3, thus excluding hysteresis effects. Although the effect is likely caused by another resistive effect, the behavior is different from the observations of the temperature dependency in Section 4.3 and therefore cannot be attributed to the electrolyte conductivity. Unfortunately, we found only little research dealing with cell dynamics and their SOC dependency in the regarded high frequency range. Typical cell dynamics such as double layer effects can be excluded because their large relaxation time cannot be assigned to the investigated high frequencies [29,42]. There are some previous studies available, which investigated Li-ion intercalation into graphite

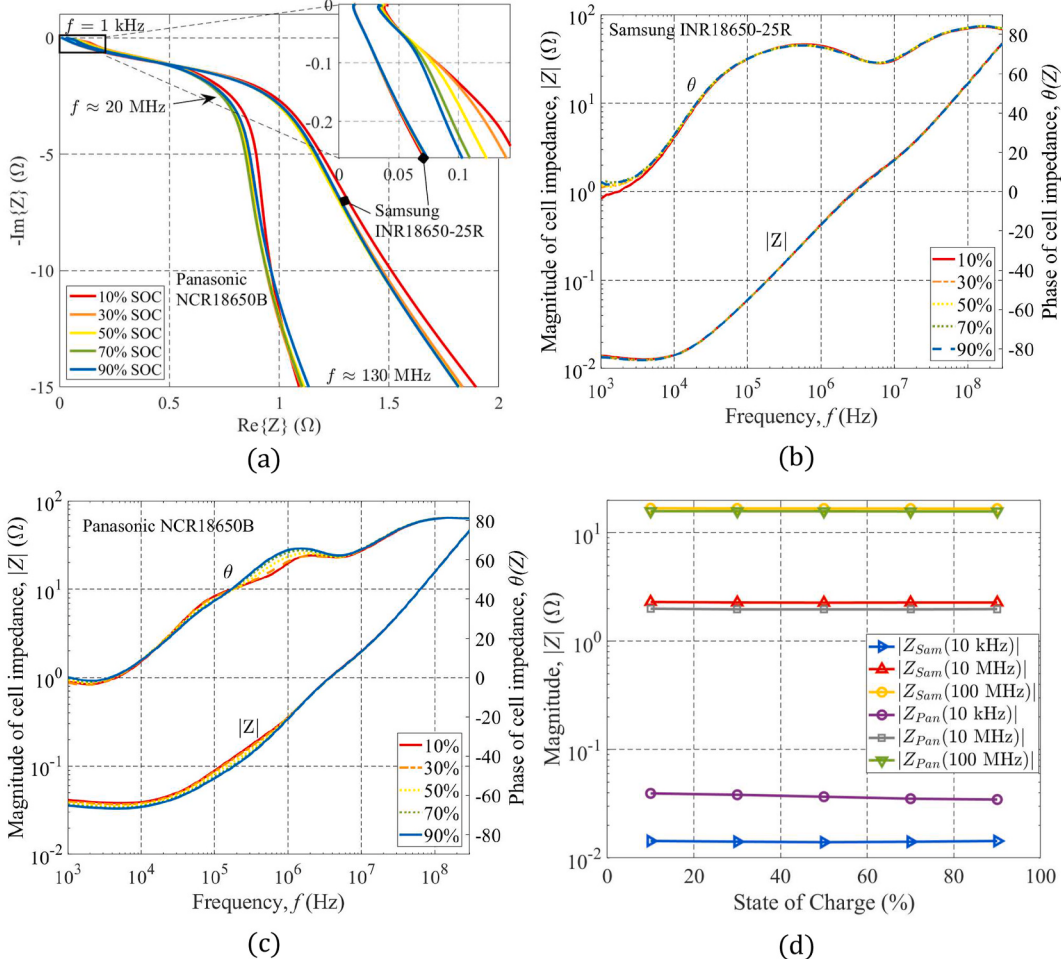


Fig. 7. SOC dependency of the cell impedance for two different cylindrical 18650 Li-ion cells: HF Nyquist plot (a) and Bode plots (b, c) of Samsung INR18650-25R and Panasonic NCR18650B, respectively. (d) Impedance of both cells over SOC for selected frequencies.

materials using EIS [45,46]. The studies could attribute the high frequency signature of the cell to contact resistance between the graphite electrode and the current collectors [45], or resistance within the bulk electrode [46]. Considering the different behavior of the Samsung INR18650-25R and the Panasonic NCR18650B, we assume that the specific cell technology including the thick electrode layers of the Panasonic cell account for the impedance change with SOC. More precisely, we suppose that the delithiation of the thick graphite anode, which dominates the volume change during cyclic conditioning [47], reduces the anode volume, leading to a higher contact resistance between active electrode and current collector.

Another reason for the increased impedance could be the additional heat resistance layer (HRL) that is inserted between negative electrode and separator of the NCR18650B [48], and the contact resistance between HRL and anode, which might depend on the volume change of the electrode, too.

Regardless of the mentioned possible reasons, for frequencies higher than 1 MHz, the additional contact or layer resistance has no more influence, because we assume that it is shunted by the fast time-varying current through capacitive coupling.

5. Conclusion

In this work, we investigated the resistive-inductive behavior of a variety of high power and high energy 18650 Li-ion cells. First in literature, we considered how cell geometry, temperature and SOC influence the cell's impedance characteristics over a wide frequency range

from 1 kHz to 300 MHz. By applying impedance measurements and modeling the cell characteristics from a physical point of view, we were able to address the following cell design aspects:

- Cylindrical high energy cells with thick electrode layers have less windings leading to a smaller jelly roll inductance than corresponding high power cells with the same tab arrangement (similar to solenoids, where $L \propto N^2$).
- The tab pattern significantly contributes to the resistive-inductive cell behavior. More windings enclosed by the tabs lead to a higher jelly roll inductance, which let the impedance significantly increase for high frequencies. More tabs along the current collectors can reduce the jelly roll inductance.
- A mandrel inserted in the center of the jelly roll was found not to influence the cell's impedance characteristics in the investigated frequency range.
- As the anodic current collector has a higher conductivity than the cathodic collector, we assume that it is the major contributor to the skin effect characteristics of the cell initiating above some megahertz.

These conclusions are linked to macroscopic cell geometry aspects and are therefore mainly independent from materials chemistry, except of a small contribution of the materials chemistry to the ohmic resistance. Besides, electrochemical reactions are regarded negligible for the HF signal response of the battery.

Considering a frequency of 10 MHz relevant for PLC, the geometrical

differences among the investigated cells lead to impedance values ranging from 1.8Ω for group D to 6.2Ω for group C cells.

Beside the cell's ohmic resistance, also the cell impedance above a frequency of 10 MHz showed a temperature dependency. This can be attributed to temperature dependent ohmic losses, which are caused by ionic current flow between the electrode layers forced by high current collector reactances. Other geometrical aspects such as current collector inductance did not show any temperature dependency. In case of the Samsung INR18650-25R, a temperature reduction from 40°C to 0°C lead to an impedance increase from 2.1Ω to 2.7Ω at 10 MHz.

It is commonly assumed that the SOC hardly influences the high frequency cell characteristics, which was also found in this work. However, one of the investigated cells exhibited a slight SOC dependency for frequencies below 1 MHz, most probably caused by anodic volume change during cyclic conditioning. Above 1 MHz, no SOC influence could be observed.

These findings can be used for predicting the influence of different cell designs on its inductance and impedance characteristics and can help for selecting the appropriate cell for applications, where HF signals are present. For future PLC design, the results can be used to optimize the PLC transceiver performance with respect to different types of cells. For example, to maximize the capacity of the PLC link, the transceiver output impedance has to be adjusted to the battery load impedance such that the PLC voltage across the battery is maximized [49]. This can be realized by an additional capacitor compensating for the positive imaginary part of the battery impedance at the PLC carrier frequency. Furthermore, the dynamic output current of the transceiver can be

adapted to a specific cell to obtain a good tradeoff between PLC channel capacity and energy consumption.

CRediT authorship contribution statement

Thomas F. Landinger: Conceptualization, Methodology, Validation, Formal analysis, Investigation, Writing - original draft, Writing - review & editing, Visualization. **Guenter Schwarzerger:** Resources, Writing - review & editing. **Andreas Jossen:** Writing - review & editing, Supervision, Project administration, Funding acquisition.

Declaration of competing interest

The authors declare that they have no known competing financial interests or personal relationships that could have appeared to influence the work reported in this paper.

Acknowledgements

The authors would like to thank Jonas Soellner and Philipp Berg of the Technical University of Munich and Markus Spielbauer of the Munich University of Applied Sciences for providing the CT scans of the cells and for helpful discussions during the process of tab identification. This work was supported by the Federal Ministry for Economic Affairs and Energy, Germany within the project LiMeSI [grant number 03ETE019A]. The responsibility of this publication stays with the authors.

Appendix A. Net inductance derivation of current collector segments

A.1 Parallel current flow (Fig. A.8a).

The voltages across the inductances of the positive (L_+) and negative (L_-) current collector segments are given by⁴

$$\begin{aligned} V_+ &= j\omega L_+ \cdot I_+ + j\omega M \cdot I_- , \\ V_- &= j\omega L_- \cdot I_- + j\omega M \cdot I_+ . \end{aligned} \quad (\text{A.1})$$

The impedance between the tabs can be expressed as

$$Z = \frac{V_+ + V_-}{I} = \frac{V_1 + V_-}{I} = Z_+ \| Z_- = \frac{Z_+ \cdot Z_-}{Z_+ + Z_-} , \quad (\text{A.2})$$

where

$$Z_+ : = \frac{V_+ + V_-}{I_+} = \frac{j\omega L_+ \cdot I_+ + j\omega M \cdot I_- + RI_+}{I_+} , \quad (\text{A.3})$$

$$Z_- : = \frac{V_1 + V_-}{I_-} = \frac{RI_- + j\omega L_- \cdot I_- + j\omega M \cdot I_+}{I_-} . \quad (\text{A.4})$$

For the common case of supposing identical inductances $L_+ = L_-$ and equally distributed R , the currents get $I_+ = I_- = I/2$, and eq (A.2) can be rearranged using (A.3) and (A.4), to

$$\frac{(j\omega L_+ + j\omega M + R) \cdot (R + j\omega L_- + j\omega M)}{j\omega L_+ + j\omega M + R + R + j\omega L_- + j\omega M} = (j\omega L_+ + j\omega M + R) \parallel (j\omega L_- + j\omega M + R) . \quad (\text{A.5})$$

For high frequencies, $R \ll \omega L$, and eq. (A.5) can be simplified to

$$Z = (j\omega L_+ + j\omega M) \parallel (j\omega L_- + j\omega M) : = j\omega L_{\text{par}} \quad (\text{A.6})$$

which solely contains the net inductance of the current collector segment:

$$L_{\text{par}} = (L_+ + M) \parallel (L_- + M) , \quad (\text{A.7})$$

As reported in Ref. [13], the inductive coupling factor $k := M / \sqrt{L_+ L_-}$ for tightly aligned current collectors is close to 1, thus the net inductance for parallel current flow is

⁴ For a better readability, the frequency dependency of the quantities voltage, current and impedance is explicitly not shown.

$$L_{+} \approx L_{-}, \quad k \approx 1$$

$$L_{par} = (L_{+} + M) \parallel (L_{-} + M) \quad \overbrace{\quad}^{(2L_{+}) \parallel (2L_{-})} = L_{+}. \quad (\text{A.8})$$

A.2 Antiparallel current flow (Fig. A.8b).

The voltages across the inductances of the positive (L_{+}) and negative (L_{-}) current collector segments are given by

$$V_{+} = j\omega L_{+} \cdot I_{+} - j\omega M \cdot I_{-},$$

$$V_{-} = j\omega L_{-} \cdot I_{-} - j\omega M \cdot I_{+}. \quad (\text{A.9})$$

Since $I_{+} = I_{-}$ and $k \approx 1$, the voltages can be calculated by

$$V_{+} \approx j\omega L_{+} \cdot I_{+} - j\omega L_{+} \cdot I_{+} = 0,$$

$$V_{-} \approx j\omega L_{-} \cdot I_{-} - j\omega L_{-} \cdot I_{-} = 0. \quad (\text{A.10})$$

Since the voltages across the inductances are zero for antiparallel current flow, the net inductance of the current collector segment is zero:

$$L_{par} : = (L_{+} - L_{-}) + (L_{+} - L_{-}) = 0. \quad (\text{A.11})$$

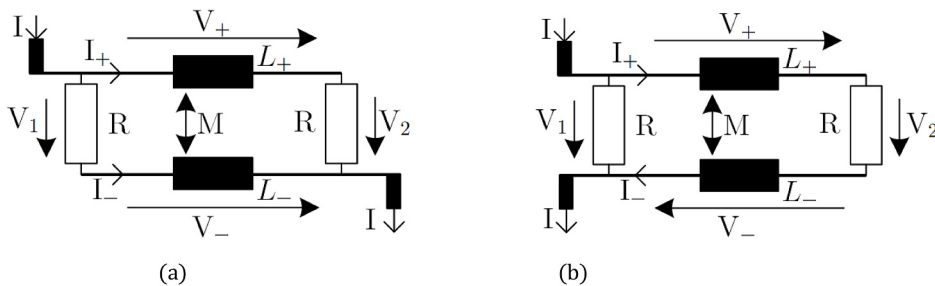


Fig. A.8. Current collector segments including mutual inductive coupling for parallel (a) and anti-parallel (b) current flow depending on the tab position. The resistances represent the resistance between positive and negative collector segments.

Appendix B. Fitting Accuracy of the EEC Model of Fig. 1a

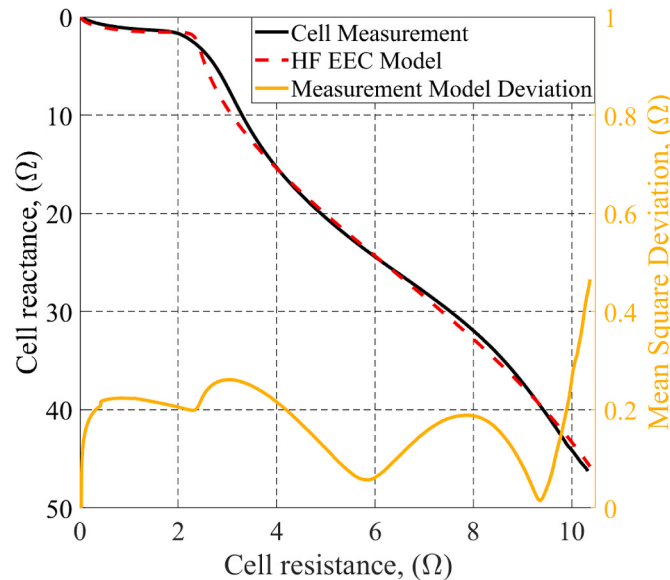


Fig. B.9. HF impedance measurement result and fitted EEC model of LG INR18650 MJ1. The mean square deviation between measurement and model is typical among the investigated cells.

References

- [1] G.E. Blomgren, The development and future of lithium ion batteries, *J. Electrochem. Soc.* 164 (2017) A5019–A5025, <https://doi.org/10.1111/j.1541-1210.2017.11011.x>.
- [2] H.J. Hong, J.R. Sevillano, C. Kain, G. Hofer, K. Felber, W.K. Chan, Alternatives in battery communication protocols, in: SAE Technical Paper Series, SAE International 400 Commonwealth Drive, Warrendale, PA, United States, 2017.
- [3] Y. Maryanka, Wiring reduction by battery power line communication, in: IEE Seminar on Passenger Car Electrical Architecture, IEE, Birmingham, UK, 21/6/2000, p. 8.
- [4] O. Opalko, Powerline-Kommunikation für Batteriemanagement-Systeme in Elektro- und Hybridfahrzeugen, KIT Scientific Publishing, Karlsruhe, 2017.
- [5] I. Ouannes, P. Nickel, K. Dostert, Cell-wise monitoring of Lithium-ion batteries for automotive traction applications by using power line communication: battery modeling and channel characterization, in: 2014 18th IEEE International Symposium on Power Line Communications and its Applications (ISPLC), Glasgow, United Kingdom, IEEE, Piscataway, NJ, 2014, pp. 24–29.

- [6] A.P. Talie, W.A. Pribyl, G. Hofer, Electric vehicle battery management system using power line communication technique, in: 2018 14th Conference on Ph.D. Research in Microelectronics and Electronics (PRIME), IEEE, Prague, 2018, pp. 225–228 [S. I], 2/7/2018 - 5/7.
- [7] C. Bolsinger, J. Brix, M. Dragan, K.P. Birke, Investigating and modeling the transmission channel of a prismatic lithium-ion cell and module for powerline communication, *Journal of Energy Storage* 10 (2017) 11–19, <https://doi.org/10.1016/j.est.2016.12.001>.
- [8] E. Barsoukov, J.R. Macdonald, *Impedance Spectroscopy*, John Wiley & Sons, Inc, Hoboken, NJ, USA, 2018.
- [9] J. Illig, J.P. Schmidt, M. Weiss, A. Weber, E. Ivers-Tiffée, Understanding the impedance spectrum of 18650 LiFePO₄-cells, *J. Power Sources* 239 (2013) 670–679, <https://doi.org/10.1016/j.jpowsour.2012.12.020>.
- [10] T.F. Landinger, G. Schwarzberger, A. Jossen, A novel method for high frequency battery impedance measurements, in: 2019 IEEE International Symposium on Electromagnetic Compatibility, Signal Integrity and Power Integrity, New Orleans, LA, USA, IEEE, [Piscataway, New Jersey], 2019, pp. 106–110.
- [11] F.C. Laman, Inductive impedance of a spirally wound Li/MoS₂ cell, *J. Electrochim. Soc.* 133 (1986) 2441, <https://doi.org/10.1149/1.2108430>.
- [12] P.J. Osswald, S.V. Erhard, A. Noel, P. Keil, F.M. Kindermann, H. Hoster, A. Jossen, Current density distribution in cylindrical Li-Ion cells during impedance measurements, *J. Power Sources* 314 (2016) 93–101, <https://doi.org/10.1016/j.jpowsour.2016.02.070>.
- [13] S. Schindler, M.A. Danzer, Influence of cell design on impedance characteristics of cylindrical lithium-ion cells: a model-based assessment from electrode to cell level, *Journal of Energy Storage* 12 (2017) 157–166, <https://doi.org/10.1016/j.est.2017.05.002>.
- [14] P. Korth Pereira Ferraz, R. Schmidt, D. Kober, J. Kowal, A high frequency model for predicting the behavior of lithium-ion batteries connected to fast switching power electronics, *Journal of Energy Storage* 18 (2018) 40–49, <https://doi.org/10.1016/j.est.2018.04.024>.
- [15] E. Hoene, S. Guttowski, R. Saikly, W. John, H. Reichl, Rf-properties of automotive traction batteries, in: IEEE International Symposium on Electromagnetic Compatibility, 2003. EMC '03, Istanbul, Turkey, vol. 1, IEEE, 2003, pp. 425–428, 16/5/2003.
- [16] T.F. Landinger, G. Schwarzberger, A. Jossen, A physical-based high-frequency model of cylindrical lithium-ion batteries for time domain simulation, *IEEE Trans. Electromagn. C* 62 (2020) 1524–1533, <https://doi.org/10.1109/TEMC.2020.2996414>.
- [17] N. Shoaib, *Vector Network Analyzer (VNA) Measurements and Uncertainty Assessment*, Springer International Publishing, Cham, s.l., 2017.
- [18] A. Jossen, Fundamentals of battery dynamics, *J. Power Sources* 154 (2006) 530–538, <https://doi.org/10.1016/j.jpowsour.2005.10.041>.
- [19] Y. Wu, S. Saxena, Y. Xing, Y. Wang, C. Li, W. Yung, M. Pecht, Analysis of manufacturing-induced defects and structural deformations in lithium-ion batteries using computed tomography, *Energies* 11 (2018) 925, <https://doi.org/10.3390/en11040925>.
- [20] M.J. Brand, *Lithium-ion Battery Cells and Systems under Dynamic Electric Loads*, Dissertation, München, 2018.
- [21] C. Ropeter, *Verhalten von Batterien bei impulsförmigen Strombelastungen unter Berücksichtigung des Skineffekts*. Zugl.: Clausthal, Techn. Univ., Diss., 2006, Shaker, Aachen, 2007.
- [22] J. Wang, K. Zou, C. Chen, L. Chen, A high frequency battery model for current ripple analysis, in: Twenty-Fifth Annual IEEE Applied Power Electronics Conference and Exposition (APEC), 2010, Palm Springs, CA, USA, IEEE, Piscataway, NJ, 2010, pp. 676–680.
- [23] J.A. Tegopoulos, E.E. Kriegis, *Eddy Currents in Linear Conducting Media*, Elsevier, Amsterdam, 1985.
- [24] M. Park, X. Zhang, M. Chung, G.B. Less, A.M. Sastry, A review of conduction phenomena in Li-ion batteries, *J. Power Sources* 195 (2010) 7904–7929, <https://doi.org/10.1016/j.jpowsour.2010.06.060>.
- [25] S.S. Zhang, K. Xu, T.R. Jow, EIS study on the formation of solid electrolyte interface in Li-ion battery, *Electrochim. Acta* 51 (2006) 1636–1640, <https://doi.org/10.1016/j.electacta.2005.02.137>.
- [26] H.A. Wheeler, Formulas for the skin effect, *Proc. IRE* 30 (1942) 412–424, <https://doi.org/10.1109/JRPROC.1942.232015>.
- [27] Agilent Technologies, Appl. Note 5989-5935EN: Ultra-low Impedance Measurements Using 2-Port Measurements, Inc., USA, 2007.
- [28] P.J. Osswald, M.d. Rosario, J. Garche, A. Jossen, H.E. Hoster, Fast and accurate measurement of entropy profiles of commercial lithium-ion cells, *Electrochim. Acta* 177 (2015) 270–276, <https://doi.org/10.1016/j.electacta.2015.01.191>.
- [29] F.M. Kindermann, A. Noel, S.V. Erhard, A. Jossen, Long-term equalization effects in Li-ion batteries due to local state of charge inhomogeneities and their impact on impedance measurements, *Electrochim. Acta* 185 (2015) 107–116, <https://doi.org/10.1016/j.electacta.2015.10.108>.
- [30] M. Guo, R.E. White, Mathematical model for a spirally-wound lithium-ion cell, *J. Power Sources* 250 (2014) 220–235, <https://doi.org/10.1016/j.jpowsour.2013.11.023>.
- [31] J.B. Quinn, T. Waldmann, K. Richter, M. Kasper, M. Wohlfahrt-Mehrens, Energy density of cylindrical Li-ion cells: a comparison of commercial 18650 to the 21700 cells, *J. Electrochim. Soc.* 165 (2018) A3284–A3291, <https://doi.org/10.1149/2.0281814jes>.
- [32] J. Ho, T.R. Jow, S.A. Boggs, Implications of advanced capacitor dielectrics for performance of metallized film capacitor windings, in: Proceedings of the 2008 IEEE International Power Modulators and High Voltage Conference, Las Vegas, NV, USA, IEEE, Piscataway, NJ, 2008, pp. 556–559.
- [33] E.B. Rosa, The self and mutual inductance of linear conductors, *Bulletin of the Bureau of Standards* 4 (2) (1908) 332–333.
- [34] F.W. Grover, *Inductance Calculations*, Dover Publications, Newburyport, 2013.
- [35] R. Zhao, J. Liu, J. Gu, The effects of electrode thickness on the electrochemical and thermal characteristics of lithium ion battery, *Appl. Energy* 139 (2015) 220–229, <https://doi.org/10.1016/j.apenergy.2014.11.051>.
- [36] N. Ida, *Engineering Electromagnetics*, Springer International Publishing, Cham, 2015.
- [37] L.H.J. Rajmakers, D.L. Danilov, J.P.M. van Lammeren, M.J.G. Lammers, P.H. L. Notten, Sensorless battery temperature measurements based on electrochemical impedance spectroscopy, *J. Power Sources* 247 (2014) 539–544, <https://doi.org/10.1016/j.jpowsour.2013.09.005>.
- [38] D. Andre, M. Meiler, K. Steiner, C. Wimmer, T. Soczka-Guth, D.U. Sauer, Characterization of high-power lithium-ion batteries by electrochemical impedance spectroscopy. I. Experimental investigation, *J. Power Sources* 196 (2011) 5334–5341, <https://doi.org/10.1016/j.jpowsour.2010.12.102>.
- [39] T.R. Jow, S.A. Delp, J.L. Allen, J.-P. Jones, M.C. Smart, Factors limiting Li + charge transfer kinetics in Li-ion batteries, *J. Electrochim. Soc.* 165 (2018) A361–A367, <https://doi.org/10.1149/2.12221802jes>.
- [40] K. Oldiges, D. Diddens, M. Ebrahiminia, J.B. Hooper, I. Cekic-Laskovic, A. Heuer, D. Bedrov, M. Winter, G. Brunklaus, Understanding transport mechanisms in ionic liquid/carbonate solvent electrolyte blends, *Phys. Chem. Chem. Phys.* 20 (2018) 16579–16591, <https://doi.org/10.1039/c8cp01485j>.
- [41] X. Zhang, Thermal analysis of a cylindrical lithium-ion battery, *Electrochim. Acta* 56 (2011) 1246–1255, <https://doi.org/10.1016/j.electacta.2010.10.054>.
- [42] J.P. Schmidt, S. Arnold, A. Loges, D. Werner, T. Wetzel, E. Ivers-Tiffée, Measurement of the internal cell temperature via impedance: evaluation and application of a new method, *J. Power Sources* 243 (2013) 110–117, <https://doi.org/10.1016/j.jpowsour.2013.06.013>.
- [43] W. Waag, S. Käbitz, D.U. Sauer, Experimental investigation of the lithium-ion battery impedance characteristic at various conditions and aging states and its influence on the application, *Appl. Energy* 102 (2013) 885–897, <https://doi.org/10.1016/j.apenergy.2012.09.030>.
- [44] C.T. Love, M.B.V. Virji, R.E. Rocheleau, K.E. Swider-Lyons, State-of-health monitoring of 18650 4S packs with a single-point impedance diagnostic, *J. Power Sources* 266 (2014) 512–519, <https://doi.org/10.1016/j.jpowsour.2014.05.033>.
- [45] Y.-C. Chang, H.-J. Sohn, Electrochemical impedance analysis for lithium ion intercalation into graphitized carbons, *J. Electrochim. Soc.* 147 (2000) 50, <https://doi.org/10.1149/1.1393156>.
- [46] M. Holzapfel, A. Martinent, F. Alloin, B. Le Gorrec, R. Yazami, C. Montella, First lithiation and charge/discharge cycles of graphite materials, investigated by electrochemical impedance spectroscopy, *J. Electroanal. Chem.* 546 (2003) 41–50, [https://doi.org/10.1016/S0022-0728\(03\)00144-X](https://doi.org/10.1016/S0022-0728(03)00144-X).
- [47] L.K. Willenberg, P. Dechen, G. Fuchs, D.U. Sauer, E. Figgemeier, High-precision monitoring of volume change of commercial lithium-ion batteries by using strain gauges, *Sustainability* 12 (2020) 557, <https://doi.org/10.3390/su12020557>.
- [48] Panasonic Industrial Devices Sales Europe, Lithium - Ion/NNP + HRL Technology: NCR18650B Datasheet.
- [49] M. de Pianta, A.M. Tonello, On impedance matching in a power-line-communication system, *IEEE Trans. Circuits Syst. II* 63 (2016) 653–657, <https://doi.org/10.1109/TCSII.2016.2530218>.